Transformation of the strengthening and toughening modes of Poly(urethane) elastomer with hard segments embracing Ti_3C_2 MXene and its excellent triboelectric performance

Chuanqiang Sun, Baogang Yuan, Zhe Han, Dezhen Yang, Jinchuan Chen, Huajie Xu*, Chuntai Liu, Changyu Shen

State Key Laboratory of Structural Analysis, Optimization and CAE Software for Industrial Equipment, National Engineering Research Center for Advanced Polymer Processing Technology, The Key Laboratory of Advanced Materials Processing & Mold of Ministry of Education, Zhengzhou University, Zhengzhou, Henan 450002, China.

***Corresponding author:** Huajie Xu.

E-mail address: xuhuajie@zzu.edu.cn, xhj1106@gmail.com (H. Xu).

1. Synthesis and characterization

1.1 Preparation of Ti_3C_2 MXene and determination of its -OH group content

The preparation of Ti_3C_2 MXene and the determination of its -OH group content is similar to Magenau method.[1] First, 2 g of LiF was dissolved in 40 mL of 9 M HCl in a Teflon beaker and stirred for 30 min. Then, 2 g of Ti_3AlC_2 powder was slowly added into the LiF/HCl acid solution and stirred at 35 ℃ for 24 h. Next, the resultant mixture was washed with deionized (DI) water continuously by centrifuging at 3500 rpm until the pH of the mixture became approximately 6. The precipitation was dispersed in anhydrous ethanol for 1 h under ultrasound in an ice water bath, and the precipitation obtained by centrifugation of the prepared solution was added to deionized water. MXene solution was obtained after centrifugation at 3500 rpm for 10 min, and MXene nanosheets were obtained after freeze-drying. In order to determine its hydroxyl group content, Ti_3C_2 MXene was modified by $C_{12}H_{25}$-NCO and the content of -OH on the surface of Ti_3C_2 MXene was determined by thermogravimetric analysis. The results show that the content of -OH on the surface of Ti_3C_2 MXene is about 1/130 mol/g.

Typically, the molar mass of the $Ti_3C_2T_z$ repeating unit ($M_{Ti3C2Tz}$) was calculated by assuming z = 2,[2] and surface composition F/O/OH = 0.25/0.5/0.25.[3,4] Using the molar mass of $C_{12}H_{25}$-NCO ($M_{C12H25\text{-}NCO}$) and the mass fraction (X_{final}) of $Ti_3C_2T_z$ in $C_{12}H_{25}$-$Ti_3C_2T_z$ obtained by thermogravimetric analysis, this ratio can be estimated using the following relationship:

$$[C_{12}H_{25}-NCO]/[Ti_3C_2T_z] = (\frac{1-X_{final}}{M_{C12H25-NCO}})/(\frac{X_{final}}{M_{Ti3C2Tz}}) \quad (1)$$

Equation 1 can be modified to calculate the ratio of grafted $C_{12}H_{25}$-NCO chains to the number of available surface functional groups ($T_{reactive}$) by including z and $X_{reactive}$ explicitly:

$$[C_{12}H_{25}-NCO]/[Ti_3C_2T_z] = (\frac{1-X_{final}}{M_{C12H25-NCO}})/(\frac{X_{final}}{M_{Ti3C2Tz}} \times z \times X_{reactive}) \quad (2)$$

Where $X_{reactive}$ refers to the concentration of reactive surface groups (-OH and O-) on $Ti_3C_2T_z$ relative to the total concentration of surface groups. If X_{final} is 0.383 and $X_{reactive}$ is 0.75, then

$$[C_{12}H_{25}-NCO]/[Ti_3C_2T_z] = (\frac{1-0.383}{211.35g/mol})/(\frac{0.383}{201.65g/mol}) = 1.54$$

$$[C_{12}H_{25}-NCO]/[T_{reactive}] = (\frac{1-0.383}{211.35g/mol})/(\frac{0.383}{201.65} \times 2 \times 0.75) = 1.02$$

1.2 Materials characterization

The morphology of Ti_3C_2 were observed by an atomic force microscope (AFM + Nano IR Bruker). X-ray diffraction (XRD) patterns were analyzed using a DX-2700BH X-ray diffractometer with Cu Ka radiation (k=1.5405 Å) within the scope of 5-35°. Attenuated total reflectance-Fourier transform infrared (ATR-FTIR) spectrum were measured by a Nicolet 6700 (Thermo, USA). All materials were scanned from 4000 to 500 cm^{-1} with a resolution of 4 cm^{-1} and a scanning time of 64. Differential scanning calorimetry (DSC) experiments were conducted using a TA Instruments Q2000 under the nitrogen atmosphere. The samples were heated from -70 ℃ to 150 ℃ with a rate of 10 ℃/min, and held isothermally for 5 minutes to eliminate any thermal history. The sample was then cooled down to -70 °C at a rate of 10 °C/min and held isothermally for 2 minutes, followed by heating up to 150 °C at a rate of 10 °C/min. All data were collected during the

second heating process. Dynamic mechanical analysis (DMA) experiments of samples with approximate sizes of 10 mm × 5 mm × 0.5 mm were conducted using a TA Q800 Instrument with a heating rate of 3 ℃/min from 30 ℃ to 100 ℃. Both 1 Hz and 10 Hz tensile frequencies were applied in a strain-controlled mode with a constant amplitude of 0.1%. The surface potential was measured by the Oscilloscope (STO1102C, Micsig).

1.3 Mechanical tests

Mechanical tensile tests were performed using an electronic universal material testing machine (UTM2203, Shenzhen Suns Technology Stock Co., Ltd., China) with a 100 N load cell at room temperature. The samples were cut into 10 × 5 × 0.5 mm. The strain rate of 50 mm/min was used for both the unidirectional stretching and loading-unloading cycles. At least three specimens were tested for each elastomer sample, and the average values with standard errors were calculated. The toughness was acquired by integrating the area under the stress-strain curves. The energy dissipation was calculated by integrating the area encompassed by the cyclic tensile curves. The damping capacity was defined as the ratio of the dissipated energy to the loading energy. For stress relaxation, the sample was rapidly stretched to a constant strain (100%), and the change in the stress over time was recorded.

1.4 Crack tolerance and Self-healing tests

The fracture energy was conducted using a tensile test on the $PUSS_2$-$MX_{0.5}$ elastomer sheets (10.0 mm in length, 5.0 mm in width, and 0.5 mm in thickness) with and without a single edged notch at a strain rate of 3 $mm \cdot min^{-1}$. The fracture toughness (G_C) was calculated by the following equation:[5]

$$G_c = \frac{6Wc}{\sqrt{\lambda_c}} \quad (3)$$

Where λ_c is the strain at break of the notched sample, c is the length of the notch, and W is the energy calculated by the integration of the stress versus strain of unnotched samples.

For self-healing tests, the specimens were cut in half and then the cut surfaces were placed in contact immediately. Then, the samples were placed at 60 ℃ for healing. The self-healing efficiency was defined as follows:[6]

$$\eta = \frac{\sigma_{healed}}{\sigma_{original}} \times 100\% \quad (4)$$

Where η is the self-healing efficiency, $\sigma_{original}$ is the tensile stress of the original sample, and σ_{healed} is the tensile stress of the healed sample.

Besides, scratching recovery tests were also performed by scratching neat films with a blade to evaluate self-healing ability. The scratch healing process was observed using an optical microscope with a heating table (OLYMPUS BX53M, Japan).

1.5 Assembly of $PUSS_2$-$MX_{0.5}$/PTFE-based TENG:

The TENG was assembled in a vertical contact-separation mode. $PUSS_2$-$MX_{0.5}$ was used as the positive friction material for the triboelectric device, while PTFE was used as the negative friction material. The $PUSS_2$-$MX_{0.5}$ and commercial PTFE films were cut into square shapes with dimensions of 2.0 × 2.0 cm^2, and two copper tapes were attached to their covered sides as electrodes. They were then individually fixed onto polymethyl

methacrylate (PMMA) plates, with four springs used to keep them separated. The $PUSS_2$-$MX_{0.5}$ layer and the PTFE layer were assembled face-to-face to ensure full contact, with a gap of approximately 5 mm maintained by the springs.

1.6 Dielectric properties of elastomer

The Dielectric properties was tested by Precision LCR tester (E4980A, Agilent).

$$\varepsilon = C \times \frac{d}{\varepsilon_0 \times S} \tag{5}$$

Where C is a capacitor that uses the material as a dielectric capacitor, ε_0 is the dielectric constant of vacuum (8.85×10^{-12} F/m), d is the sample thickness, S is the sample area ($S = \pi \times 12.5^2 \times 10^{-6}$ m^2).

Calculation details: All DFT calculations are performed in ORCA software, using B3LYP functional calculations, DFT-D3 (BJ) for dispersion correction, and ma-def2-TZVP base set for dipole moment calculations.[7,8]

1.7 Output performance of TENG

The output performance of TENG was recorded by the Oscilloscope (STO1102C, Micsig) and electrochemical workstation (CHI660E, China) at room temperature and 25% RH humidity. The conductive tape and copper wires were contacted with friction layers for electrical signal output. To evaluate the output performance of TENG, the samples ($20 \times 20 \times 0.5$ mm^3) were prepared to assemble TENG for testing. The power density is determined by the following equation:

$$P = \frac{UI}{A} \tag{6}$$

Where U, I and A represent the output voltage, output current, and contact area, respectively.

2. Figures and Tables

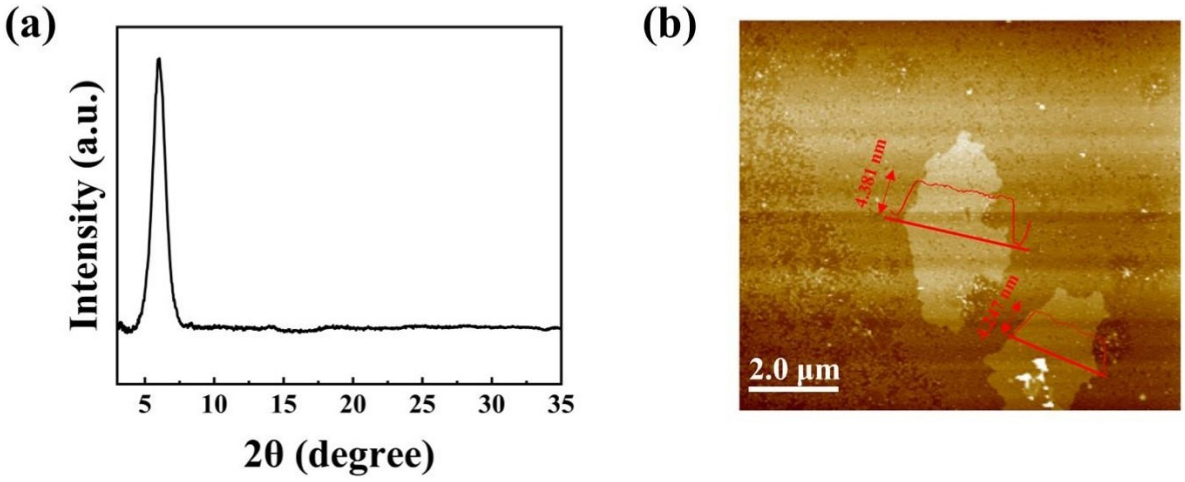

Fig. S1. (a) Wide angle X-ray diffraction pattern of Ti_3C_2 MXene and (b) AFM image of Ti_3C_2 nanosheets.

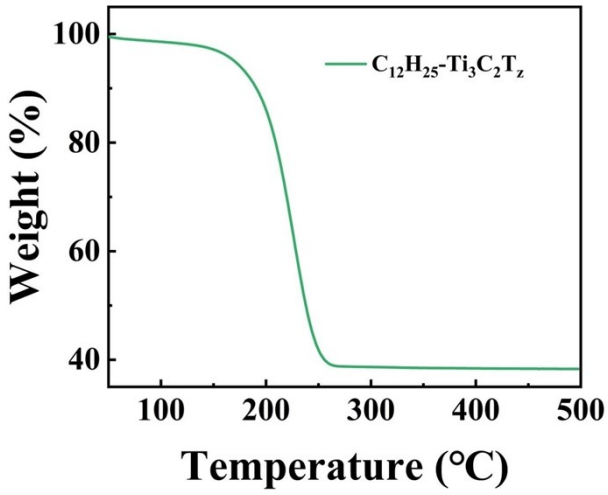

Fig. S2. TGA curve of $C_{12}H_{25}$-$Ti_3C_2T_z$.

Table. S1. The ratio of reactants for different elastomers.

Samples	PCL (g)	IPDI (g)	MXene (mg)	4AD (g)	n (-OH+-NH_2) / n (-NCO)
PU-MX_0	10.00	1.11	/	/	1
PU-$MX_{0.5}$C	10.00	1.16	55.80	/	1
PU-MX_1C	10.00	1.21	112.00	/	1
PU-MX_5C	10.00	1.61	580.30	/	1
PU-$MX_{0.5}$H	10.00	1.11	55.60	/	1
PU-MX_1H	10.00	1.11	111.10	/	1
PU-MX_5H	10.00	1.11	555.50	/	1
$PUSS_1$-$MX_{0.5}$	10.00	2.28	67.60	1.24	1
$PUSS_{1.5}$-$MX_{0.5}$	10.00	2.84	73.50	1.86	1
$PUSS_2$-$MX_{0.5}$	10.00	3.40	79.40	2.48	1
$PUSS_{2.5}$-$MX_{0.5}$	10.00	3.96	85.30	3.10	1

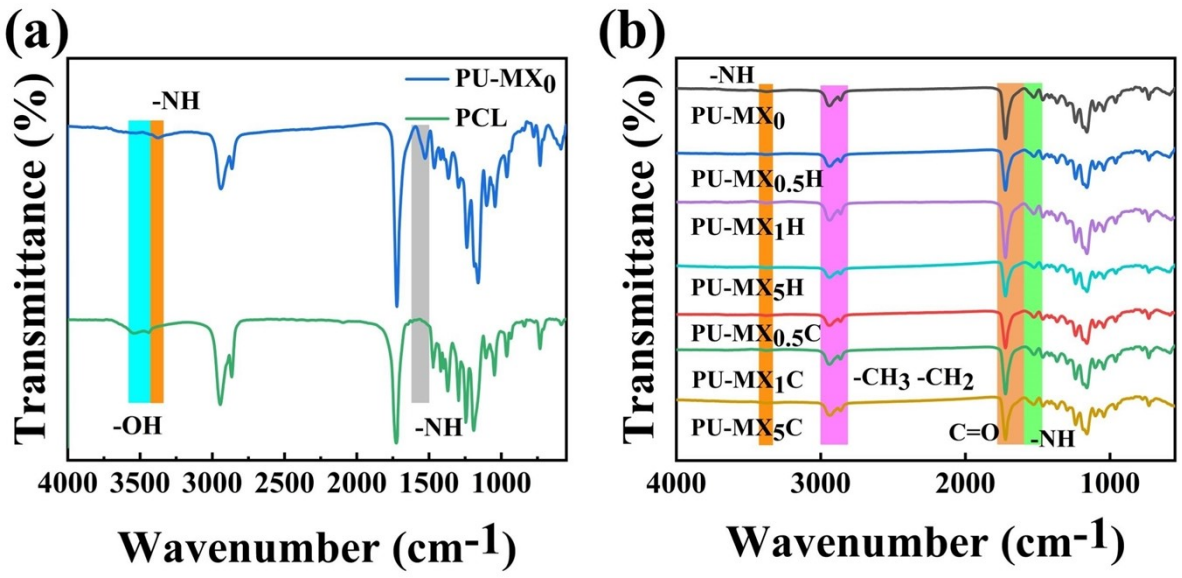

Fig. S3. FT-IR spectra of (a) PU-MX_0 and PCL and (b) PU-MX.

Table. S2. Physical properties of seven elastomers.

Sample	T_g (°C)	T_c (°C)	ΔH_c (J/g)	T_m (°C)	ΔH_m (J/g)	ΔH (ΔH_m - ΔH_c)
PU-MX_0	-55.40	0.66	28.21	34.92	34.91	6.70
PU-$MX_{0.5}C$	-55.28	-11.17	27.38	32.25	34.98	7.60
PU-MX_1C	-55.40	7.96	10.21	33.05	13.58	3.37
PU-MX_5C	-55.27	9.99	5.54	32.15	7.80	2.26
PU-$MX_{0.5}H$	-56.25	-12.19	24.39	35.93	42.10	17.71
PU-MX_1H	-55.26	-12.07	25.75	33.51	39.29	13.54
PU-MX_5H	-55.52	-3.72	28.21	33.51	33.11	4.90

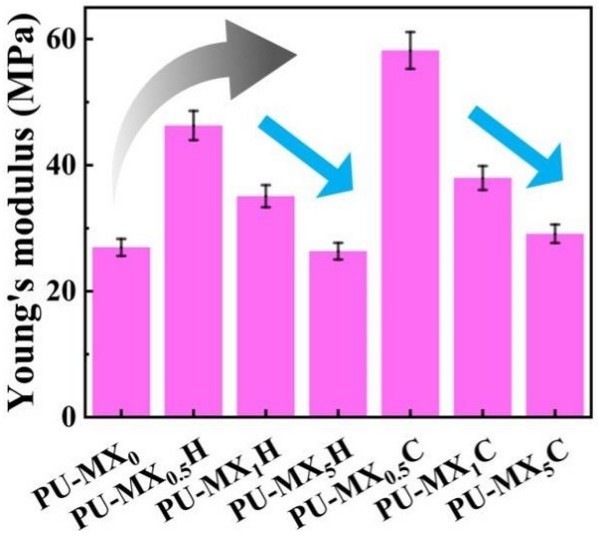

Fig. S4. Young's modulus of PU-MX_0, PU-MXH and PU-MXC elastomers.

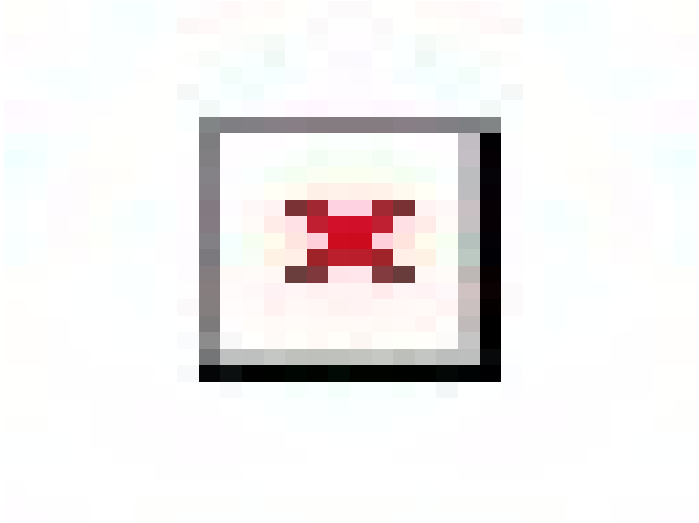

Fig. S5. Wide angle X-ray diffraction patterns of PU-MX_0, PU-MXH and PU-MXC.

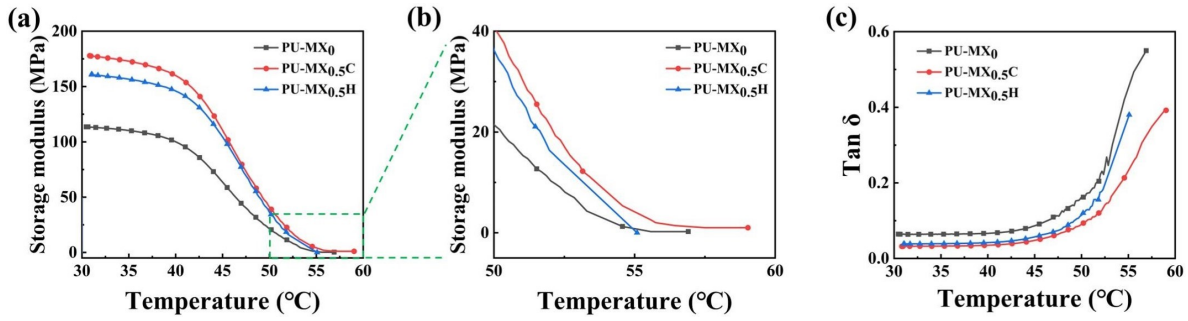

Fig. S6. (a) Storage modulus and (b) partial enlargement, (c) Tan δ of PU elastomers.

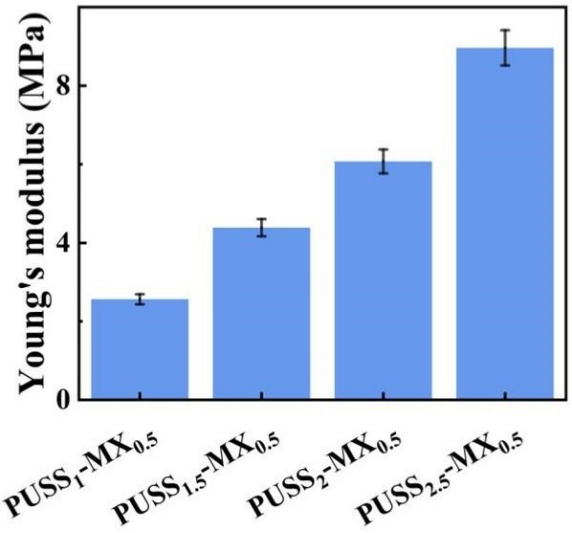

143

144 **Fig. S7.** Young's modulus of PUSS-MX elastomers.

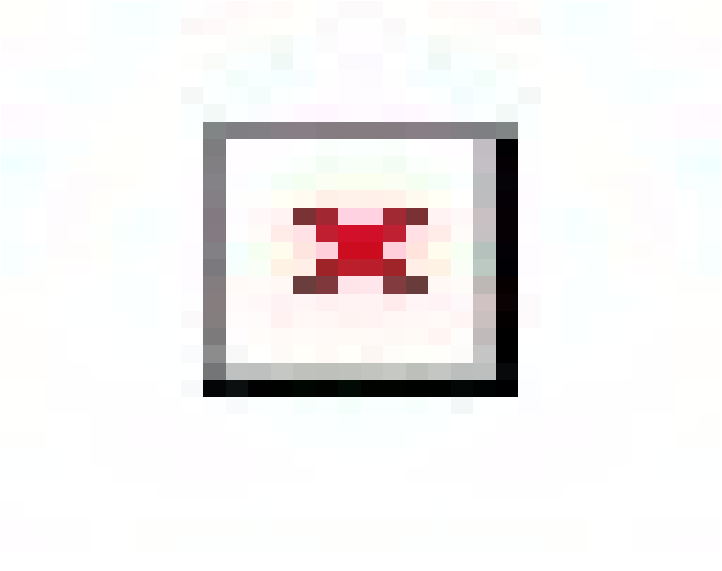

145

146 **Fig. S8.** DSC curves of PUSS-MX.

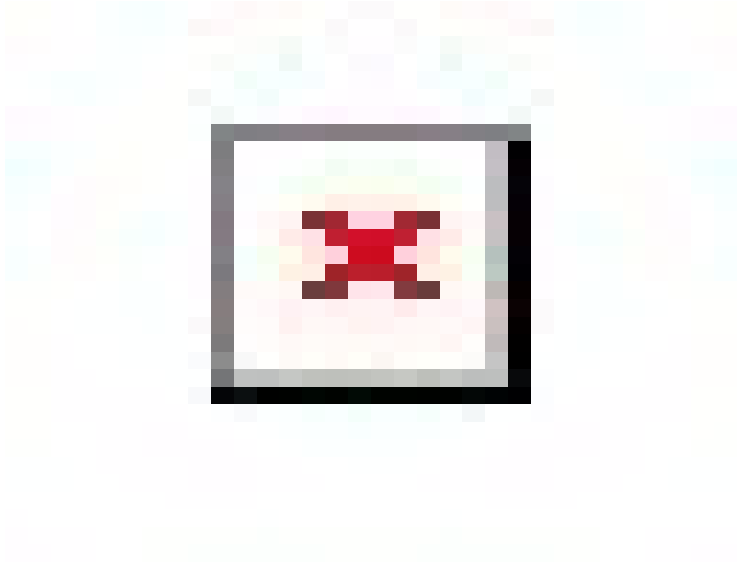

Fig. S9. FT-IR spectra of PUSS-MX in the wavenumber range of 4000-600 cm^{-1}.

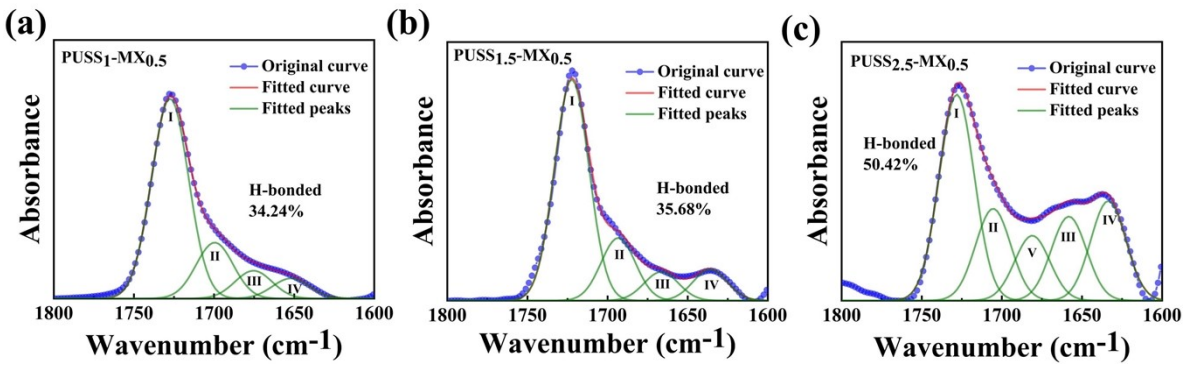

Fig. S10. Deconvolution of C=O stretching region in FT-IR spectra of three elastomers.

Table. S3. Summary of the assignment of the deconvoluted subpeaks in the FT-IR C=O absorption bands for four elastomers.

Assignment		Wavenumber (cm^{-1})				Area (%)			
		$PUSS_1$ -$MX_{0.5}$	$PUSS_{1.5}$ -$MX_{0.5}$	$PUSS_2$ -$MX_{0.5}$	$PUSS_{2.5}$ - $MX_{0.5}$	$PUSS_1$ -$MX_{0.5}$	$PUSS_{1.5}$ -$MX_{0.5}$	$PUSS_2$ -$MX_{0.5}$	$PUSS_{2.5}$ -$MX_{0.5}$
υ (C=O) urethane amide	Free	1727	1722	1725	1728	65.76	64.32	53.64	37.69
	H-bonded (Ordered)	1699	1693	1700	1705	18.42	18.24	20.55	16.81
υ(C=O) urea amide	Free	-	-	-	1680	-	-	-	11.89
	H-bonded (Disordered)	1675	1666	1668	1658	9.16	8.37	8.97	15.38
	H-bonded (Ordered)	1651	1635	1631	1633	6.66	9.07	16.84	18.23
Total degree of H-bonded						34.24	35.68	46.36	50.42

Table S4. Comparison of Tensile strength, Elongation, and Toughness of various self-healing polymers.

Self-healing motif	Tensile strength (MPa)	Elongation (%)	Toughness (MJ m^{-3})	Ref
Disulfides	6.76	923	26.9	9
	4.3	128	3.1	10
	0.392	202	0.5	11
	0.23	105	0.13	12
	0.46	932	1.87	13
	6.3	852	23.2	14
Hydrogen bonding	1.9	780	10.0	15
	1.7	1735	14.9	16
	1.9	1508	17.6	17
	3.4	600	8	18
Boronic ester	4.4	58	1.4	19
	2.1	450	6.0	20
Van der Waals	4.4	560	12.0	21
Ionic interactions	10.3	366	29.0	22
	5.2	1667	40.1	23
Boroxine	12.7	184	17.5	24
Boronic ester and H-bonds	1.64	777	-	25
Disulfides and H-bonds	0.81	3100	13	26
	9.3	637	-	27
	14.08	974.84	64.6	28
	22.1	**2281.4**	**334.3**	**This work**

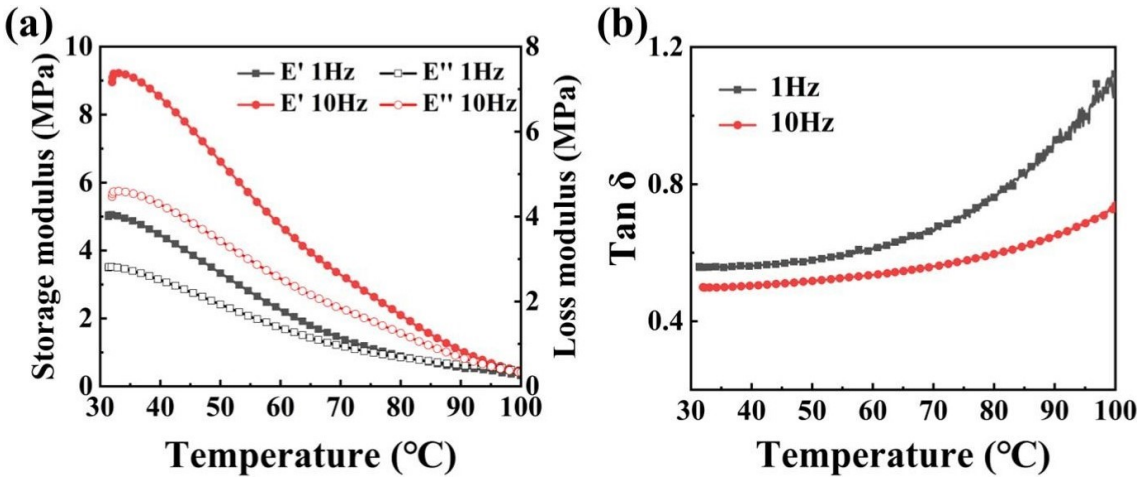

Fig. S11. Dynamic mechanical tests of $PUSS_2$-$MX_{0.5}$ elastomer at 1 Hz and 10 Hz.

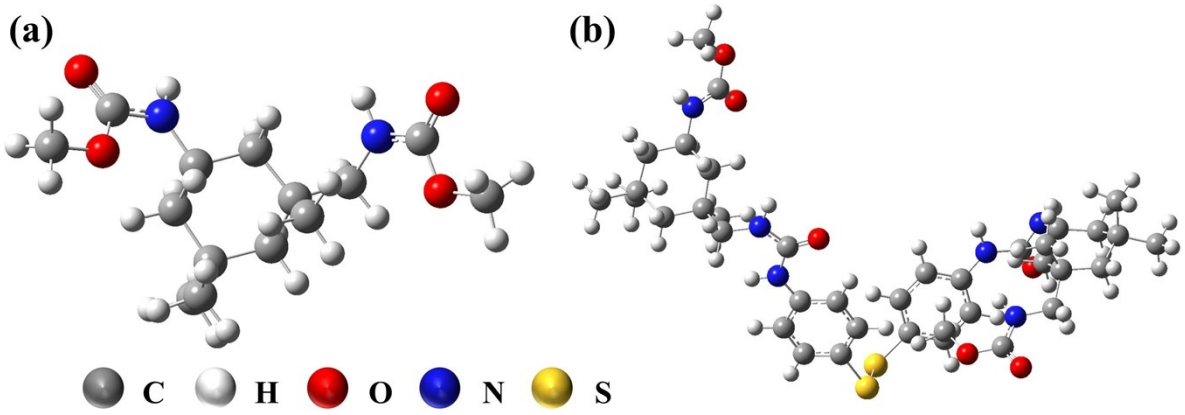

Fig. S12. Structure optimization models of (a) urethane group and (b) urea group.

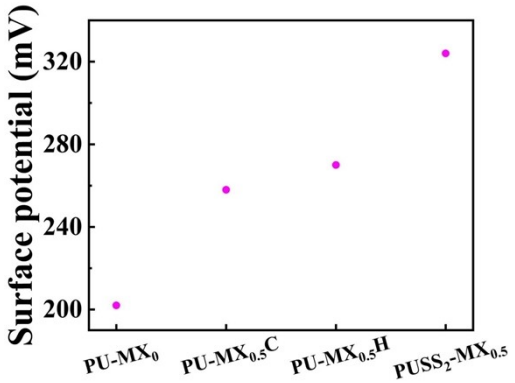

Fig. S13. Surface potential measurement of elastomers.

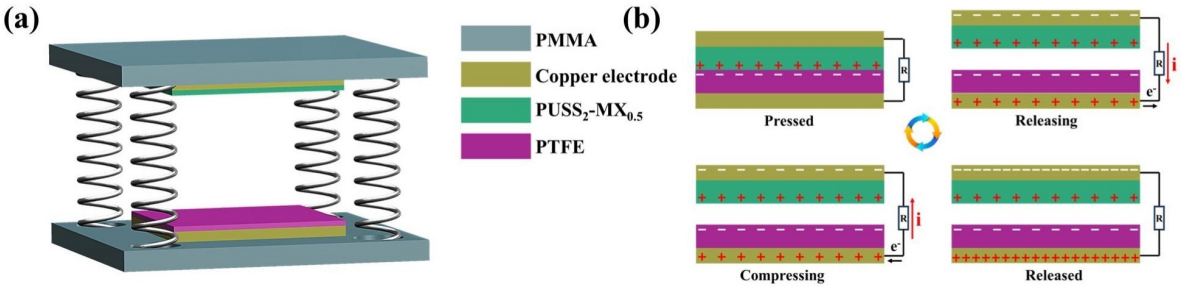

Fig. S14. Illustration of (a) assembly and (b) working principle of the $PUSS_2$-$MX_{0.5}$-TENG.

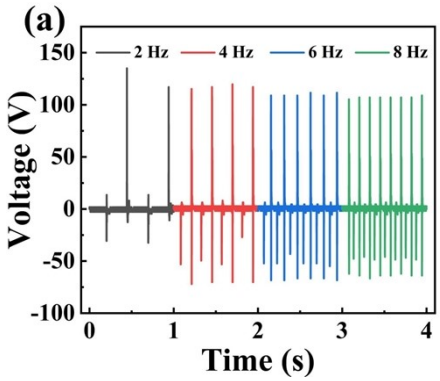

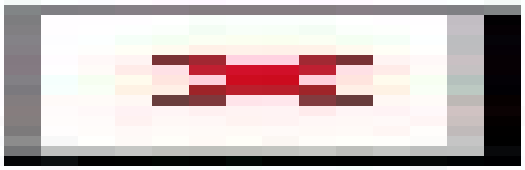

Fig. S15. (a) Output voltage of $PUSS_2$-$MX_{0.5}$ TENG at the different testing frequency, (b) Output voltage of the TENG in the continuous running more than 6000 cycles.

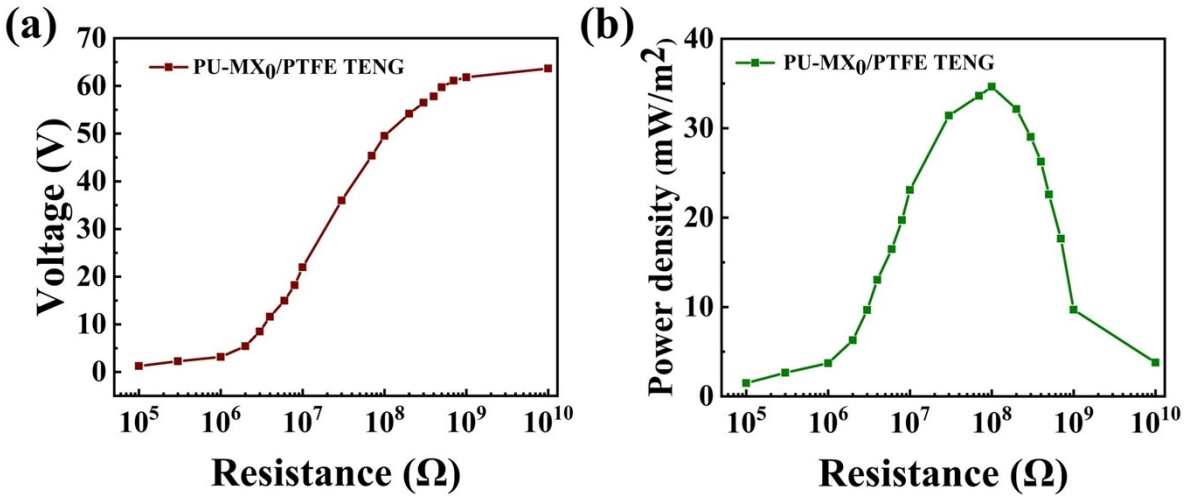

Fig. S16. (a) Voltage and (b) power density of PU-MX_0/PTFE TENG connected to different load resistance.

Table S5. Comparison of Open circuit voltage and Power density of various TENGs.

Component	Open circuit voltage (V)	Open circuit voltage per unit area (V/cm^2)	Power Density(mW/m^2)	Ref
PVDF/PTFE	25	6.25	2.75	29
H-DLC/PTFE	32	2.53	57	30
woven-TENG/PTFE	62.9	0.98	5.43	31
(BMOF/FCF)/(PTFE/Al)	47	20.89	1.1	32
(MXene/PLA)/PTFE	88	22	35.4	33
ZnO-PVDF/Au/PTFE	97	53.88	245	34
$PUSS_2$-$MX_{0.5}$/PTFE	**119**	**29.75**	**76.2**	**This work**

Video S1. Green light-emitting diodes (LEDs) powered by the TENG.

References

1. R. M. McDaniel, M. S. Carey, O. R. Wilson, M. W. Barsoum and A. J. D. Magenau, Chemistry of Materials, 2021, 33, 1648-1656.
2. P. O. Å. Persson and J. Rosen, Current Opinion in Solid State and Materials Science, 2019, 23, 100774.
3. R. Ibragimova, M. J. Puska and H.-P. Komsa, ACS Nano, 2019, 13, 9171-9181.
4. T. Hu, M. Hu, B. Gao, W. Li and X. Wang, The Journal of Physical Chemistry C, 2018, 122, 18501-18509.
5. H. W. Greensmith, Journal of Applied Polymer Science, 1963, 7, 993-1002.

6. S. Park, G. Thangavel, K. Parida, S. Li and P. S. Lee, Advanced Materials, 2019, 31, 1805536.

7. F. Neese, WIREs Computational Molecular Science, 2018, 8, e1327.

8. S. Grimme, S. Ehrlich and L. Goerigk, Journal of Computational Chemistry, 2011, 32, 1456-1465.

9. S. M. Kim, H. Jeon, S. H. Shin, S. A. Park, J. Jegal, S. Y. Hwang, D. X. Oh and J. Park, Advanced Materials, 2018, 30, 1705145.

10. R. H. Aguirresarobe, L. Martin, M. J. Fernandez-Berridi and L. Irusta, EXPRESS POLYMER LETTERS, 2017, 11, 266-277.

11. Y. Amamoto, H. Otsuka, A. Takahara and K. Matyjaszewski, Advanced Materials, 2012, 24, 3975-3980.

12. Z. Q. Lei, H. P. Xiang, Y. J. Yuan, M. Z. Rong and M. Q. Zhang, CHEMISTRY OF MATERIALS, 2014, 26, 2038-2046.

13. Y. Wang, X. K. Liu, S. H. Li, T. Q. Li, Y. Song, Z. D. Li, W. K. Zhang and J. Q. Sun, ACS APPLIED MATERIALS & INTERFACES, 2017, 9, 29120-29129.

14. Y. L. Chen, A. M. Kushner, G. A. Williams and Z. B. Guan, NATURE CHEMISTRY, 2012, 4, 467-472.

15. J. H. Kang, D. Son, G. J. N. Wang, Y. X. Liu, J. Lopez, Y. Kim, J. Y. Oh, T. Katsumata, J. W. Mun, Y. Lee, L. H. Jin, J. B. H. Tok and Z. N. Bao, ADVANCED MATERIALS, 2018, 30.

16. Y. X. Pan, J. L. Hu, Z. Y. Yang and L. Tan, ACS APPLIED POLYMER MATERIALS, 2019, 1, 425-+.

17. P. Cordier, F. Tournilhac, C. Soulié-Ziakovic and L. Leibler, NATURE, 2008, 451, 977-980.

18. Y. Yang, F. S. Du and Z. C. Li, ACS APPLIED POLYMER MATERIALS, 2020, 2, 5630-5640.

19. J. J. Cash, T. Kubo, A. P. Bapat and B. S. Sumerlin, Macromolecules, 2015, 48, 2098-2106.

20. C. Kim, H. Ejima and N. Yoshie, JOURNAL OF MATERIALS CHEMISTRY A, 2018, 6, 19643-19652.

21. A. Susa, R. K. Bose, A. M. Grande, S. van der Zwaag and S. J. Garcia, ACS APPLIED MATERIALS & INTERFACES, 2016, 8, 34068-34079.

22. J. Y. Zhang, M. M. Huo, M. Li, T. Q. Li, N. X. Li, J. C. Zhou and J. Jiang, POLYMER, 2018, 134, 35-43.

23. Y. Miwa, J. Kurachi, Y. Kohbara and S. Kutsumizu, COMMUNICATIONS CHEMISTRY, 2018, 1.

24. C. Y. Bao, Y. J. Jiang, H. Y. Zhang, X. Y. Lu and J. Q. Sun, ADVANCED FUNCTIONAL MATERIALS, 2018, 28.

25. J. H. Zhang, L. M. Cao and Y. K. Chen, EUROPEAN POLYMER JOURNAL, 2022, 168.

26. A. Rekondo, R. Martin, A. R. de Luzuriaga, G. Cabañero, H. J. Grande and I. Odriozola, MATERIALS HORIZONS, 2014, 1, 237-240.

27. B. Cheng, X. Lu, J. H. Zhou, R. Qin and Y. L. Yang, ACS SUSTAINABLE CHEMISTRY & ENGINEERING, 2019, 7, 4443-4455.

28. Y. W. Xu, S. Zhou, Z. H. Wu, X. Y. Yang, N. Li, Z. H. Qin and T. F. Jiao, CHEMICAL ENGINEERING JOURNAL, 2023, 466.

29. J. Zhu, Y. Zhu and X. Wang, Advanced Materials Interfaces, 2018, 5, 1700750.

30. S. H. Ramaswamy, J. Shimizu, W. Chen, R. Kondo and J. Choi, Nano Energy, 2019, 60, 875-885.

31. W. Paosangthong, M. Wagih, R. Torah and S. Beeby, Nano Energy, 2022, 92, 106739.

32. N. Jayababu and D. Kim, Nano Energy, 2021, 89, 106355.

33. Z. Du, G. Zhang, K. Chen, C. Zhou, X. Zhu, Y. Zhang, K. Chen, H.-Y. Mi, Y. Wang, C. Liu and C. Shen, ACS Appl. Mater. Interfaces, 2022, 14, 14607-14617.

34. H. H. Singh and N. Khare, Nano Energy, 2018, 51, 216-222.